Available online at www.sciencedirect.com
ScienceDirect
Journal of Power Sources 175 (2008) 127–136
JOURNAL OF POWER SOURCES
www.elsevier.com/locate/jpowsour

An approach to modeling two-phase transport in the gas diffusion layer of a proton exchange membrane fuel cell

Tetsuya Koido *, Toru Furusawa, Koji Moriyama

Fundamental Technology Research Center, Honda R&D, Co. Ltd., 1-4-1 Chuo, Wako-shi, Saitama 351-0193, Japan

Received 12 July 2007; received in revised form 6 September 2007; accepted 11 September 2007
Available online 15 September 2007

Abstract

A series of analysis methods is proposed to simulate the liquid–gas two-phase and multi-component transport phenomena in the gas diffusion layer (GDL) of a proton exchange membrane fuel cell (PEMFC). These methods involve measuring and predicting the two-phase flow properties of a GDL, and simulating the two-phase multi-component transport in the GDL. The capillary pressure is measured by the porous diaphragm method and predicted by the pore network model. The relative permeability is measured by the steady-state method and predicted by a combination of the single-phase and the two-phase lattice Boltzmann method. And the simulation of the liquid–gas two-phase transport is done using the multi-phase mixture model. The methods are applied to a carbon-fiber paper GDL to identify the two-phase multi-component transport in the GDL.
© 2007 Elsevier B.V. All rights reserved.

Keywords: PEMFC; Mathematical modeling; Two-phase flow; Gas diffusion layer

1. Introduction

Development of proton exchange membrane fuel cells (PEMFCs) has been accelerating for automotive applications since the late 1990s. Water management is a crucial factor in improving fuel cell performance, which is affected by flooding, gas dilution, and membrane dehydration. Reliability of the polymer membrane and the catalyst layer is also affected by the presence of water [1]. Among water management issues, liquid–gas two-phase flow in the gas diffusion layer (GDL) of PEMFCs is an important phenomenon because it affects the amount of water in the catalyst layer and membrane, and affects reactant transport from the gas channels to the catalyst layer.

Since the GDL of a PEMFC is usually made of electrically conductive and opaque material such as carbon fiber, it is hard to visualize or measure the liquid condition, phase velocity, and species concentration in the GDL. Various simulation efforts have been attempted to elucidate the two-phase transport phenomena in the GDL [2–12] since Wang et al. [2] first introduced the concepts of capillary pressure and relative permeability to describe two-phase flow in fuel cell GDL assuming Darcy's law.

In general, capillary pressure and relative permeability are regarded as the dominant properties of the liquid–gas two-phase flow characteristics in a porous medium [13]. Liquid water is driven by capillary pressure, which is defined as the difference between the gas and liquid phase pressures:

$$P_c = P_g - P_l. \tag{1}$$

As the liquid phase pressure changes with the void space occupied by liquid water, the capillary pressure depends on the liquid saturation, s, defined as the liquid volume fraction of the total pore space in the porous medium:

$$s = \frac{V_l}{V_{pore}}. \tag{2}$$

Darcy's law can be extended for two-phase flow in porous media as described in the following equation:

$$u_g = \frac{Kk_{rg}}{\mu_g L}\Delta P_g, \qquad u_l = \frac{Kk_{rl}}{\mu_l L}\Delta P_l, \tag{3}$$

where k_r is the relative permeability of each phase defined as the ratio of the permeability of the phase at a given saturation level to the absolute permeability of the porous medium.

Although a fundamental understanding of two-phase flow in a GDL is of great importance in analyzing the effect of the flood-

* Corresponding author. Tel.: +81 48 461 2511; fax: +81 48 462 5090.
E-mail address: tetsuya_koido@n.f.rd.honda.co.jp (T. Koido).

0378-7753/$ – see front matter © 2007 Elsevier B.V. All rights reserved.
doi:10.1016/j.jpowsour.2007.09.029

Nomenclature

C	molar concentration (mol m^{-3})
Ca	capillary number
D	mass diffusivity of species (m^2 s^{-1})
$\mathbf{e}$	lattice velocity vector
f	distribution function
$\mathbf{F}$	total interaction force
$\mathbf{F}_1$	interaction force between fluid–fluid
$\mathbf{F}_2$	interaction force between fluid–solid
$\mathbf{F}_3$	body force
$\mathbf{g}$	body force per unit mass
$g_{k\bar{k}}$	interactive strength between phases k and $\bar{k}$
g_{ks}	interactive strength between k phase and solid phase
G	Green's function
$\mathbf{j}_l$	mass flux of liquid phase (kg m^{-2} s^{-1})
I	current density (A m^{-2})
k, $\bar{k}$	phase
k_r	relative permeability
K	permeability (m^2)
L	length (m)
M	molecular weight (kg mol^{-1})
n	mass flux (kg m^{-2} s^{-1})
n_s	index for solid wall
N	connectivity number
P	pressure (Pa)
r	pore curvature (m)
R	gas constant, 8.134 J mol^{-1} K^{-1}
Re	Reynolds number
s, s_l	saturation of liquid water
t	time
T	temperature (K, °C)
u, $\mathbf{u}$	velocity (m s^{-1}) or non-dimensional
$\mathbf{u}'$	common velocity
V	volume (m^3)
$\mathbf{x}$	location vector
$\mathbf{x}'$	neighboring site of $\mathbf{x}$
x, y, z	in direction x, y, z

Greek symbols

β	net water molar flux per proton molar flux through a PEM
γ	convection corrector factor
ε	porosity
λ	mobility of a phase
μ	viscosity (kg m^{-1} s^{-1})
θ_c	contact angle (°)
ν	kinematic viscosity (m^2 s^{-1})
ρ	density (kg m^{-3})
σ	surface tension force (N m^{-1}) or non-dimensional
τ	relaxation time

Subscripts

a	unknown value
c	capillary
eff	effective
eq	equilibrium
g	gas phase
i	direction
Int	intrinsic
l	liquid phase
pore	pore in a porous medium
s	solid phase
sat	saturated value
0	reference state

Superscripts

H_2O	water
N_2	nitrogen
O_2	oxygen
α	species

ing phenomenon on the PEMFC performance, only a limited number of studies on two-phase flow property measurements for a GDL used in a PEMFC have been published [14,15]. As an alternative approach, the properties have been empirically derived from lithological experiments [1,13,16–18]. The simulations presented in Refs. [2–12] have been attempted with those properties from porous media other than an actual GDL as stated above. It is therefore desirable to identify a method that can elucidate the phenomena in GDL resulting from the effects of such properties as the fibrous structure and wettability.

2. Measurement and prediction methods

This present study uses a carbon-fiber paper as the GDL material that has been treated with a 5 wt.% solution of polytetra-fluoro-ethylene (PTFE) because a GDL is commonly a porous medium whose porosity is high enough for gas transport, with highly hydrophobic wettability, which allows for easy drainage of liquid water. Fundamental properties of the GDL were obtained by general measurement methods: the contact angle, porosity, pore size distribution, and absolute permeability were, respectively, measured by the Wilhelmy or droplet method, pycnometer method, mercury porosimetry, and capillary flow porosimetry [19].

The following subsections describe a series of analysis methods to elucidate the transport phenomena in a GDL. These methods involve measuring the two-phase flow properties of a GDL, predicting those properties, and simulating the two-phase multi-species transport in a GDL.

2.1. Capillary pressure measurement

Fig. 1 shows a schematic diagram of a device for measuring the capillary pressure versus saturation (P_c–s) curve that is based on the porous diaphragm method [13,20]. A Toray TGP-H type carbon-fiber GDL disk sample is placed inside the chamber, and sealing materials are applied on top and bot-

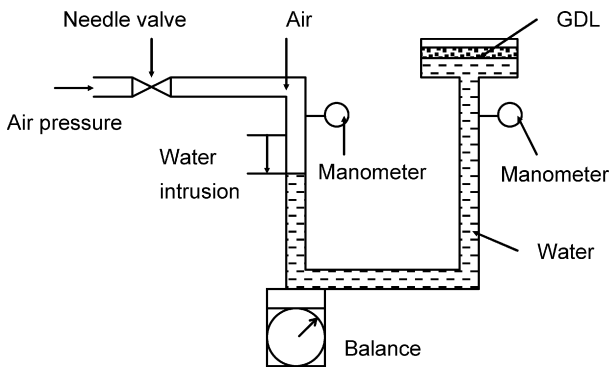

Fig. 1. Schematic diagram of P_c–s curve measurement device.

tom surfaces of the sample near the perimeter in order it does not interfere with liquid imbibition. Liquid water is forced into the porous sample from below by air pressure at room temperature. The measurement is started by monitoring an abrupt change of the liquid water pressure when we observe, thorough the transparent sample holder, air bubbles in the liquid water below the sample disappear. The capillary pressure and saturation are, respectively, measured from the liquid water pressure and amount of water contained in the pore space of the sample. The measurement is done after it is confirmed that the value of the liquid pressure has stabilized within a range that the value does not affect the P_c–s curve. The P_c–s curve is determined by repeating this liquid water imbibition procedure in small increments at each state until liquid water penetrates the GDL. The gas phase pressure in the calculation of capillary pressure is assumed to be the atmospheric pressure. The saturation is determined by precisely measuring the mass of liquid water forced into the GDL sample and calculating the ratio of the liquid water volume converted from this liquid water mass to the total pore volume.

2.2. Capillary pressure prediction

We applied pore network model [21,22] to predict the P_c–s curve of the GDL for two reasons. Firstly, the approach does not require high computational cost because the model idealizes the pore morphology and topology as a pore network consisting of pores and throats. Secondly, the GDL properties, such as wettability, pore size distribution, and pore connectivity, are easily modified as parameters in the calculation. This approach is applicable because the process of a phase intrusion can be regarded as quasi-static at each saturation value. On the other hand, the relative permeability calculation, described in the latter section, requires consider the flow in an actual complex structure to estimate the pressure drop. The pore network can be constructed based on the pore size distribution of the GDL as measured by mercury porosimetry (Fig. 2) and the connectivity number. The connectivity number is extracted by applying an image processing technique that employs a thinning algorithm [23,24] to the image that has been obtained by the microfocal X-ray CT of the carbon-fiber paper GDL. The resolution of the image is 1 μm. Fig. 3 shows the image of the Toray TGP-H-060 GDL, which consists of non-woven carbon fibers each with a

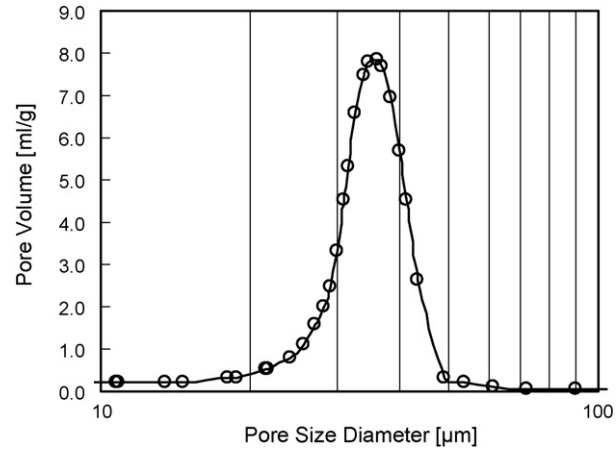

Fig. 2. Pore size distribution of GDL (Toray TGP-H-060).

diameter of about 7 μm, and the respective porosity is 0.79. The x-axis in the figure shows the thickness direction of the GDL, which we believe to be the dominant direction in terms of transport between the gas channel and the catalyst layer. As seen in the figure, the fibers are stacked in layers in the x direction, and no particular structural difference can be seen in the y and z directions. Thus, we assumed that the GDL shows different permeability in the x direction, but that it has the same permeabilities in the y and z directions. For the above reason, we have measured or predicted absolute and relative permeability in the x direction. Fig. 4 shows the result of applying the thinning algorithm. The gray objects show the fibrous structure of the GDL, and the distributed dots show the skeleton of the pore network, the flow paths in the GDL. The connectivity number is calculated by counting the average number of skeleton lines at each connection point. The pore network consists of 120 pores in each of 3 directions (120 × 120 × 120). And the diameter of each pore is determined by random number based on the pore size distribution. The throats are also generated by random num-

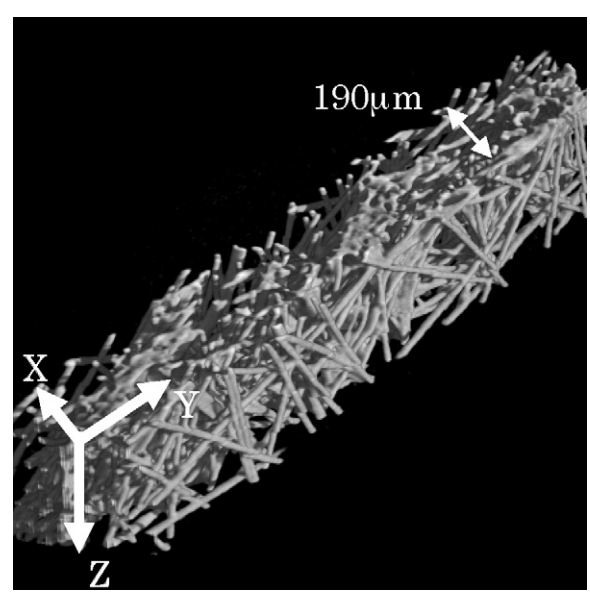

Fig. 3. Microfocal X-ray CT image of carbon paper (Toray TGP-H-060).

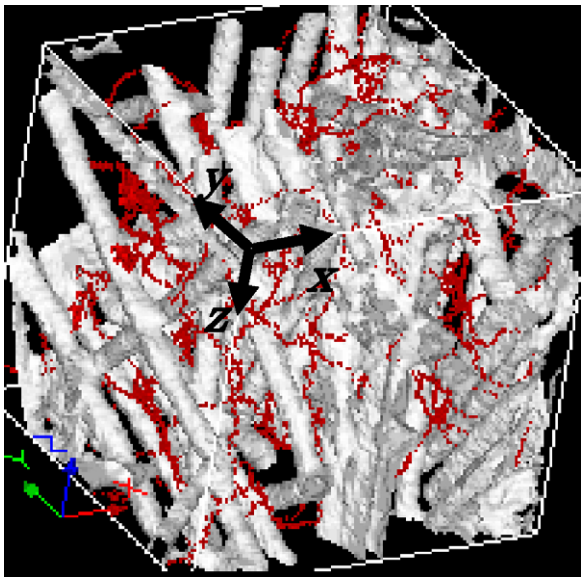

Fig. 4. Skeleton of pore network in microfocal X-ray CT image of GDL (Toray TGP-H-060). Analyzed region 120 μm^3 in size.

ber in order that the averaged number of throats corresponds to the connectivity number.

Applying the Young–Laplace law as in Eq. (4) to the pore network enables the P_c–s curve to be calculated:

$$P_c = \frac{2\sigma \cos\theta_c}{r}. \quad (4)$$

The contact angle, pore curvature based on the pore size distribution, and surface tension of water are used in this equation. Water is forced from the inlet to the outlet of this pore network according to Eq. (4). Calculation parameters are described in Table 1. The contact angle is the advancing contact angle measured by the Wilhelmy method. We chose this method because we assumed that the advancing contact angle is appropriate for this liquid intrusion process.

As an example, Fig. 5 shows the water intrusion behavior in the pore network with contact angle $\theta_c = 162°$ at $s = 0.091$ and $P_c = 6805$ Pa. It can be seen that there are some points where liquid water has been deeply infiltrates, which may lead to liquid water breakthrough at low saturation level.

2.3. Relative permeability measurement

Various measurements of relative permeability have been conducted by the steady-state test method for reservoir rock, sand stone, and other porous media [25–27]. We also used the steady-state method to measure the relative permeability of the gas phase. A schematic drawing of the test apparatus is shown in Fig. 6. A Toray TGP-H type carbon-fiber GDL test piece is

Table 1
Calculation parameters for pore network model

Contact angle, θ_c (°)	162
Surface tension, σ (N m^{-1})	70.25×10^{-3}
Connectivity number, N	4.9

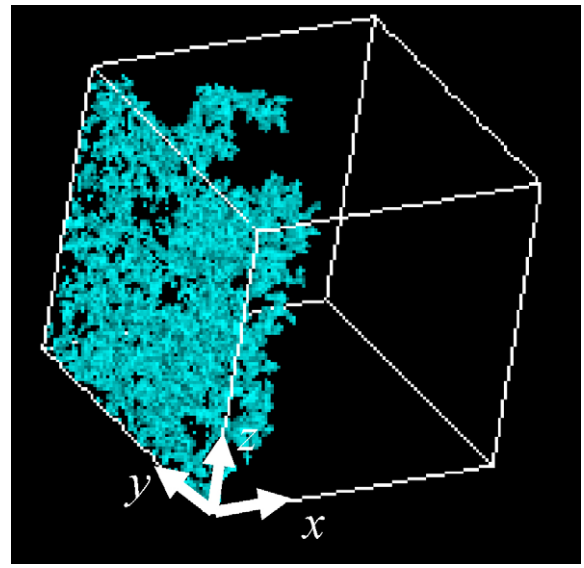

Fig. 5. Water distribution in GDL in applied pore network model ($\theta_c = 162°$).

sandwiched between similar GDLs on the inlet and outlet sides. The GDL on the inlet side ensures homogeneous distribution of liquid water in the planar direction, while the one on the outlet side minimizes the effect of the outflow boundary. Liquid is injected first and then a constant flow rate of air is established at room temperature. The pressure difference is measured after the pressure is stabilized. The GDL test piece is removed immediately after the pressure measurement so that the weight can be measured to deduce the saturation. The measured pressure difference, air flow rate, and saturation are combined as in Eq. (3) with the absolute permeability measured by capillary flow porosimetry to derive the relative permeability of the gas phase. The relative permeability of the gas phase versus saturation (k_{rg}–s) curve can be obtained in this manner.

2.4. Relative permeability prediction

The two-phase lattice Boltzmann method (TLBM) can be a useful tool for studying the complex behavior of two-phase flow,

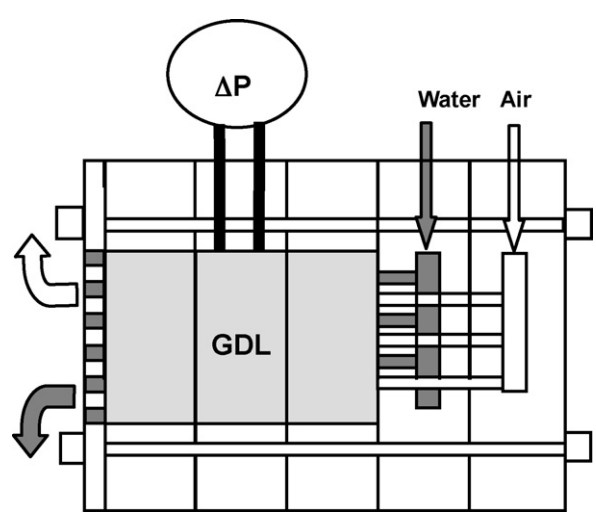

Fig. 6. Schematic diagram of relative permeability measurement device.

Table 2
Calculation conditions for SLBM used in Steps 2, 4, and 5

Property	Value
Velocity model	D3Q15 model
Calculation domain, $Lx \times Ly \times Lz$ (μm)	$122 \times 122 \times 122$
Density of gas, ρ_g (kg m^{-3})	1.0
Density of liquid, ρ_l (kg m^{-3})	1000
Viscosity of gas, μ_g (Pa s)	21×10^{-6}
Viscosity of liquid, μ_l (Pa s)	370×10^{-6}
Inlet velocity, u_x (m s^{-1})	7.0×10^{-4}

such as coalescence and the breakup of water in a porous medium with the Young–Laplace law [28]. Although it is possible to simulate the arbitrary contact angle and capillary number of a water droplet by applying TLBM to GDL, it is difficult to represent the real properties of liquid water and air at the same time in complex geometry [29]. Such properties include the viscosity, density, and surface tension. To resolve this issue, we propose a method that combines TLBM described in Refs. [28–31] and the single-phase lattice Boltzmann method (SLBM) described in Ref. [32] to predict the relative permeabilities of both phases versus the saturation of GDL (k_{rg}–s, k_{rl}–s). The method is described by the following steps:

- Step 1: reconstructing a voxel image of a GDL from microfocal X-ray slice images.
- Step 2: calculating the absolute permeability of the voxel image by the SLBM approach. Details of the conditions are shown in Table 2. Inlet velocity is specified for this step.
- Step 3: calculating the two-phase flow by the TLBM approach. The governing equations for the TLBM are tabulated in Table 3 and the Green's functions are adjusted to have specified contact angles beforehand. Details of the conditions are shown in Table 4. With these parameters, the order of capillary number Ca based on the velocity and viscosity of the liquid phase is less than 10^{-5} and Reynolds numbers for both phases Re_l, and Re_g based on the mean pore diameter are less than 10^{-2}. These are set in order that surface tension force is more predominant than viscous force and the flow can be treated as Darcy's flow. These assumptions are based on rough estimation of those non-dimensional numbers at actual fuel cell operating condition. A body force is applied as the driving force and the periodic boundary condition is applied. The water distribution in the GDL can then be obtained at a certain saturation level.
- Step 4: in calculating the permeability for the water distribution obtained in Step 3 by the SLBM approach, liquid water and fibers are regarded as solid in this step. The relative permeability of the gas phase (k_{rg}) can then be obtained by calculating the ratio between this permeability and the absolute permeability calculated in Step 1.
- Step 5: performing similar calculations for the relative permeability of the liquid phase (k_{rl}). The gas phase and fibers are regarded as solid in this step.

Table 4
Calculation conditions for TLBM used in Step 3

Property	Value (in lattice units)
Velocity model	D3Q15 model
Calculation domain, $Lx \times Ly \times Lz$	$122 \times 122 \times 122$
Density of gas, ρ_g	80
Density of liquid, ρ_l	160
Viscosity of gas, μ_g	16.7 (relaxation time of gas, $\tau_g = 1.15$)
Viscosity of liquid, μ_l	50.1 (relaxation time of liquid, $\tau_l = 1.44$)
Contact angle, θ_c	135° (interaction strength regarding wettability, $g_{gs} = -g_{ls} = -0.025$)
Surface tension, σ	18.92 (interaction strength regarding the surface tension, $g_{k\bar{k}} = 0.001$)
Body force, g_x	0.001

Fig. 7 shows the fibrous structure and water distribution in GDL when liquid saturation $s = 0.216$ in Step 3. For the reason stated in Section 2.2, we have measured or predicted absolute and relative permeability in the x direction. We assume that the computational domain size is examined. It is because the porosity of the domain matches to the macroscopic averaged value of the whole domain, and the absolute permeability calculated by SLBM on this computational domain also agreed with the value estimated from manufacturer's data.

Table 3
Governing equations for TLBM

Equations	Value (k = l, g)
Lattice Boltzmann equation	$f_i^k(\mathbf{x}+\mathbf{e}_i, t+1) - f_i^k(\mathbf{x}, t) = -\frac{f_i^k(\mathbf{x},t) - f_i^{k(\mathrm{eq})}(\mathbf{x},t)}{\tau_k}$
Macroscopic velocity	$\rho_k \mathbf{u}_k^{\mathrm{eq}} = \rho_k \mathbf{u}' + \tau_k \mathbf{F}_k$, where $\mathbf{u}' = \frac{\sum_k \rho_k \mathbf{u}_k/\tau_k}{\sum_k \rho_k/\tau_k}$, $\mathbf{u}_k = \sum_i \frac{f_i^k(\mathbf{x},t)\mathbf{e}_i}{\rho_k}$, and $\mathbf{F}_k = \mathbf{F}_{1k} + \mathbf{F}_{2k} + \mathbf{F}_{3k}$
Fluid/fluid interaction	$\mathbf{F}_{1k}(\mathbf{x}) = -\rho_k(\mathbf{x}) \sum_{x'} \sum_{\bar{k}} G_{k\bar{k}}(\mathbf{x}, \mathbf{x}') \rho_{\bar{k}}(\mathbf{x}')(\mathbf{x}' - \mathbf{x})$, where $G_{k\bar{k}}(\mathbf{x}, \mathbf{x}') = \begin{cases} g_{k\bar{k}} & \lvert\mathbf{x}-\mathbf{x}'\rvert = 1 \\ g_{k\bar{k}}/\sqrt{3} & \lvert\mathbf{x}-\mathbf{x}'\rvert = \sqrt{3} \\ 0 & \text{otherwise} \end{cases}$
Fluid/solid interaction	$\mathbf{F}_{2k}(\mathbf{x}) = -\rho_k(\mathbf{x}) \sum_{x'} G_{ks}(\mathbf{x}, \mathbf{x}') n_s(\mathbf{x}')(\mathbf{x}' - \mathbf{x})$, where $n_s = \begin{cases} 1 & \text{solid} \\ 0 & \text{fluid} \end{cases}$ and $G_{ks}(\mathbf{x}, \mathbf{x}') = \begin{cases} g_{ks} & \lvert\mathbf{x}-\mathbf{x}'\rvert = 1 \\ g_{ks}/\sqrt{3} & \lvert\mathbf{x}-\mathbf{x}'\rvert = \sqrt{3} \\ 0 & \text{otherwise} \end{cases}$
Body force	$\mathbf{F}_{3k} = \rho_k \mathbf{g}$

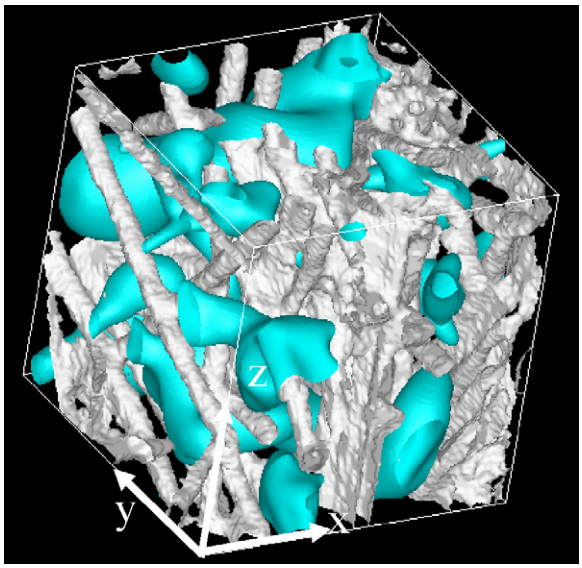

Fig. 7. Fibrous structure and water distribution in GDL using TLBM. $s = 0.216$, 120 μm^3 computational region. It flows along with x direction.

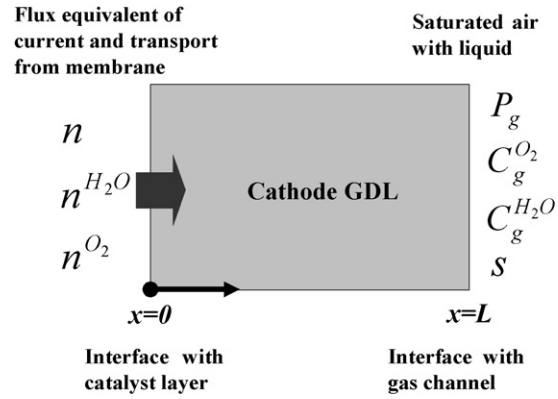

Fig. 8. 1D computational region and boundary conditions of transport simulation. Mass fluxes applied to continuity equation, water mixture equation, and oxygen equation at $x = 0$. Gas phase pressure, oxygen concentration, gas phase water concentration, and saturation are specified at $x = L$. Computational region divided into 100 control volumes.

2.5. Transport simulation

Our two-phase flow simulation model is based on the multi-phase mixture model developed by Wang and Cheng [16]. It solves a set of macroscopic equations for multi-phase multi-component flow in a porous medium and can simulate the two-phase flow and species transport in a GDL. In this study, the equations are arranged for a steady-state isothermal immiscible two-phase system involving a liquid water phase and gas phase, which consists of oxygen, water vapor, and nitrogen as shown in Table 5. Physical values without subscript, which are density, velocity, concentration, pressure, and viscosity, are for the mixture of the gas and liquid phases as defined in the table. The velocities in the formulation are superficial velocities in a porous medium. Gravity is neglected since pore size is so small, as shown in Fig. 2, that the capillary effect is dominant. And the effective gas phase diffusion coefficient is modified by the porosity as given in the following equation:

$$D_g^{\alpha,\mathrm{eff}} = \varepsilon^{1.5} D_g^{\alpha}. \tag{5}$$

The set of equations in Table 5 employs Darcy's law for each phase as described in Eq. (3), and assumes interfacial thermal and chemical equilibrium between the phases. The saturation, which is calculated by the liquid water concentration, affects the capillary pressure, and the relative permeability. The equations can be arranged in a simple mathematical form that is suitable for numerical simulation and are implemented in a 3D numerical solver of advection diffusion equations based on the finite volume method described in Ref. [33].

A steady-state 1D computation was carried out for a cathode GDL with boundary conditions for water generation and oxygen consumption corresponding to current density I at one end ($x = 0$) and fixed pressure, fixed species concentration, and fixed liquid saturation at the other end ($x = L$) as shown in Fig. 8. The physical properties, dimensions, and boundary condition values are summarized in Table 6. The capillary pressure and relative permeability characteristics (P_c–s, k_{rg}–s, and k_{rl}–s) of the Toray TGP-H type GDL were applied as empirical correlation with saturation and will be described in Section 3. The absolute permeability is measured by the capillary flow porosimetry. Values for the oxygen diffusion coefficient, liquid water viscosity, liquid water density, and gas viscosity were taken from the literature [4]. The computational region is divided into 100 equally

Table 5
Governing equations for liquid–gas two-phase mixture with oxygen and nitrogen in gas phase and phase changing water

Governing equation (phase $k = l$, g)	
Continuity	$\nabla \cdot (\rho \mathbf{u}) = 0$, where $\rho = \sum_k \rho_k s_k$, $\rho_g = \sum_\alpha C_g^\alpha M^\alpha$, $\rho \mathbf{u} = \sum_k \rho_k \mathbf{u}_k$, $s_l = \frac{C^{H_2O} - C_{sat}^{H_2O}}{C_l^{H_2O} - C_{sat}^{H_2O}}$, and $C_l^{H_2O} = \frac{\rho_l}{M^{H_2O}}$
Momentum	$\frac{1}{\varepsilon}\left[\frac{1}{\varepsilon}\nabla \cdot (\rho \mathbf{u}\mathbf{u})\right] = \nabla \cdot (\mu_{eff} \nabla \mathbf{u}) - \nabla P - \frac{\mu}{K}\mathbf{u}$, where $\mu = \rho\nu$, $\nu = \left(\sum_k \frac{k_{rk}}{\nu_k}\right)^{-1}$, $\nabla P = \sum_k \lambda_k \nabla P_k$, and $\lambda_k = \frac{k_{rk}}{\nu_k}\nu$
Species	$\alpha = O_2, H_2O$: $\nabla \cdot (\gamma_\alpha \mathbf{u} C^\alpha) = \nabla \cdot [\varepsilon D_g^{\alpha,\mathrm{eff}}(1 - s_l)\nabla C_g^\alpha] - \nabla \cdot \left[\left(\frac{C_l^\alpha}{\rho_l} - \frac{C_g^\alpha}{\rho_g}\right)\mathbf{j}_l\right]$, where $C^\alpha = \sum_k C_k^\alpha s_k$,
	$\gamma_{H_2O} = \frac{\rho}{C^\alpha}\left(\frac{1}{M^\alpha}\lambda_l + \frac{C_g^\alpha}{\rho_g}\lambda_g\right)$, $\gamma_{\alpha \neq H_2O} = \frac{\rho\lambda_g}{\rho_g(1 - s_l)}$, $C_l^{H_2O} = \frac{\rho_l}{M^{H_2O}}$, $C_l^{\alpha \neq H_2O} = 0$, $\mathbf{j}_l = K\frac{\lambda_g\lambda_l}{\nu}\frac{\partial p_{cgl}}{\partial s_l}\nabla s_l$, and $P_c = P_g - P_l$
	$\alpha = N_2$: $C_g^{N_2} = \frac{p_g}{RT} - C_g^{O_2} - C_g^{H_2O}$

Table 6
Physical properties, dimensions, and boundary conditions

Property	Value
GDL thickness, L (μm)	200
GDL porosity, ε	0.8
GDL absolute permeability, K (m^2)	9×10^{-12}
Saturated water vapor concentration, $C_{sat}^{H_2O}$ (mol m^{-3})	16.1
Temperature, T (°C)	80
Net water transport coefficient, β	0.5
Gas pressure at $x = L$, $P_g\|_{x=L}$ (Pa)	202,650
Oxygen concentration at $x = L$, $C_g^{O_2}\|_{x=L}$ (mol m^{-3})	11.2
Saturation at $x = L$, $s\|_{x=L}$	0.2
Current density, I (A m^{-2})	20,000

spaced control volumes. The net water flux transferred through the membrane from anode to cathode is assumed to be constant and the water mass flux at $x = 0$ yields

$$n^{H_2O} = \left(\frac{1}{2} + \beta\right) \frac{IM^{H_2O}}{F}. \quad (6)$$

It should be noted that variables that are solved here are the mixture of the gas and liquid phases and boundary conditions are applied as the appropriate mixture value. In case of the pressure boundary condition, the liquid phase pressure at the gas channel end ($x = L$) is higher than the gas phase pressure by the capillary pressure as in Eq. (7):

$$P_l|_{x=L} = P_g|_{x=L} - P_c(s|_{x=L}). \quad (7)$$

This can be implemented by applying an appropriate mixture pressure P, which can be evaluated by the definition in Table 5, as the boundary condition. Note also that the combined mass flux of water and oxygen is applied to the continuity equation at $x = 0$.

3. Results and discussion

3.1. Capillary pressure

Fig. 9 shows a comparison of the measured results for the Toray TGP-H type carbon-fiber paper GDL with the calculated results. The experiments were repeatedly performed on samples that had been treated with 5 wt.% solution of PTFE. The repeated experiments showed similar P_c–s curves, though some variation occurred due to the difficulty in measuring the small amount of liquid saturation. A typical result is shown in the figure. The data is plotted only to $s = 0.1$. This is because, during the experiments, we observed liquid droplets penetrated to the top surface of the sample within the liquid saturation range from 0.1 and 0.2. And it could not be clearly determined by observation at what saturation the breakthrough occurred. The calculation was performed using a pore network model with the GDL properties.

It can be seen from the comparison that the calculated data are similar to the measured data in magnitude, shape and breakthrough point of the P_c–s curve. The curve near the breakthrough point has a gentle slope, indicating that the liquid water could easily intrude when the capillary pressure would reach near the breakthrough point. Since the majority of pores in the GDL are

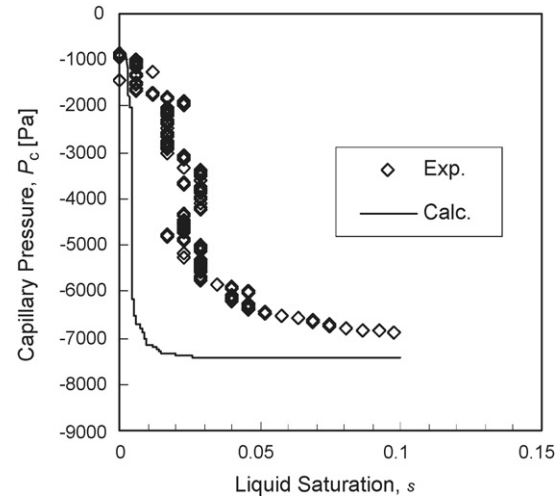

Fig. 9. Comparison of measured capillary pressure with calculated data.

concentrated in the vicinity of the most frequent pore diameter from the mercury porosimetry data (Fig. 2), this corresponds to the breakthrough capillary pressure.

The calculation method was therefore successful in expressing a P_c–s curve using the GDL properties, thus leading to a physical interpretation of the relationships between the GDL properties and the curve. Furthermore, the simulation method is able to predict the P_c–s curve for GDLs of various properties, such as wettability, pore size distribution, and pore connectivity.

3.2. Relative permeability

A comparison between the calculated relative permeability (k_{rg}–s and k_{rl}–s) and experimental relative permeability data (k_{rg}–s) is presented in Fig. 10. A Toray TGP-H type GDL treated with a 5 wt.% solution of PTFE was used for this experiment and calculation. In contrast with capillary pressure prediction, static contact angle $\theta_c = 135°$, measured by the droplet method, was used in this simulation (Table 4) because dynamic contact angles

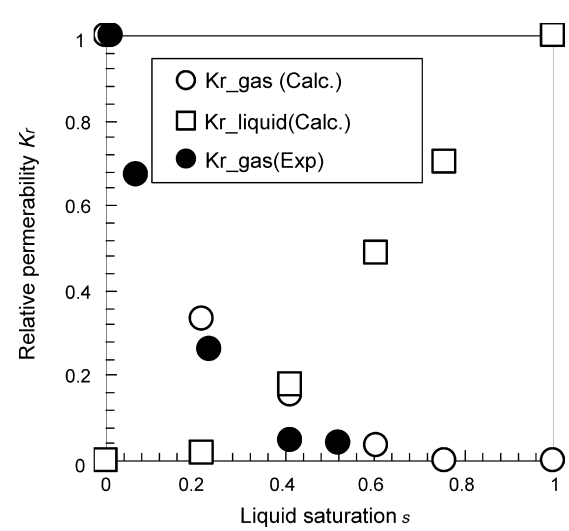

Fig. 10. Comparison of measured relative permeability with calculated data.

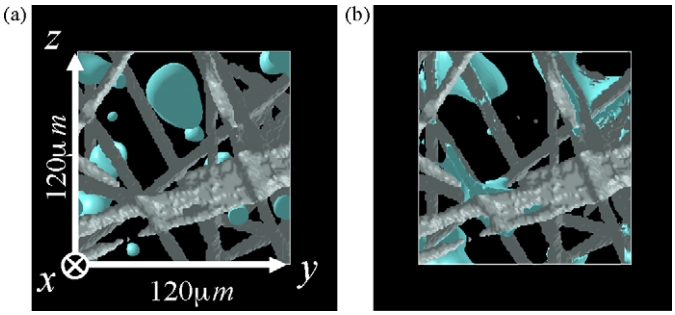

Fig. 11. Cross-sectional images of water distribution in GDL: (a) hydrophobic case ($\theta_c = 135°$) and (b) hydrophilic case ($\theta_c = 45°$).

such as advancing and receding contact angles are spontaneously represented as a numerical artifact by the TLBM approach. The accuracy of these contact angles is not examined at this point. The relative permeability of the liquid phase near $s = 0$, and that of the gas phase near $s = 1$, could not be predicted by this simulation; this was because the paths of the liquid phase in the GDL were not connected at a low level of saturation from the inlet to outlet, and the paths of the gas phase were not connected at a high level of saturation from the inlet to outlet. In other words, there is a possibility that non-connectivity of the liquid phase observed in TLBM leads to negligible relative permeability in the low saturation range.

The predicted gas phase relative permeability correctly captured the shape of the curve of the measured results and showed a similar magnitude to those at a low level of saturation. It is obvious that the absolute permeability of GDL can be estimated with SLBM correctly. And it can be assumed that the path of the gas phase in GDL is formed correctly because the relative permeability of the gas phase is agreed with experiment. In other words, the liquid path in GDL is well represented as well. We therefore assumed that the prediction method can be applied to the relative permeability of the liquid phase successfully.

To see the effect of wettability on the liquid formation in detail, TLBM computation was performed for different contact angles. Fig. 11 shows the effect of wettability on the liquid water distribution in the GDL; Fig. 11(a) shows a cross-sectional image of the water distribution in a hydrophobic GDL with contact angle $\theta_c = 135°$ (already shown in Fig. 7), while Fig. 11(b) shows this in a hypothetical hydrophilic GDL with contact angle $\theta_c = 45°$ at the same saturation level. It can be seen that liquid water tended to be present in large pores as spheres in the hydrophobic GDL, and in small pores as thin films in the hydrophilic GDL. This can be explained as follows. When the gas phase pressure is assumed to be constant, the liquid phase pressure in a small pore is lower than that of a large pore from Eqs. (1) and (4). The low liquid phase pressure in the small pore draws liquid from big pores. On the contrary, the liquid phase pressure is higher in a small pore for the hydrophobic case. And it pushes out the liquid phase to big pores. In other words, the wetting phase, which is the liquid phase in hydrophilic case and the gas phase in hydrophobic case, tends to stay in small pores.

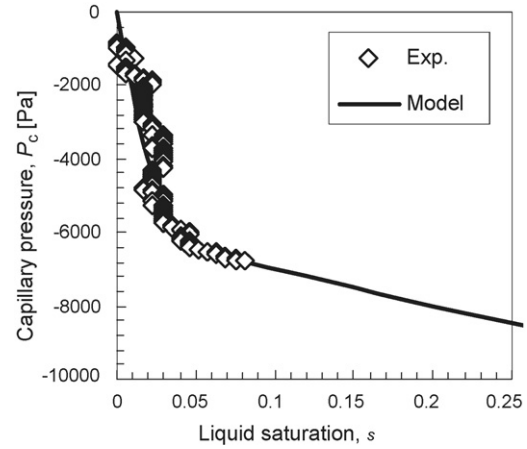

Fig. 12. Measured capillary pressure and correlated model.

3.3. Transport simulation

The empirical equations for capillary pressure and relative permeability were formulated by correlating the measured P_c–s data from Fig. 9 with the measured k_{rg}–s data from Fig. 10, and with the predicted k_{rl}–s data also from Fig. 10. These correlated models were then applied to a numerical computation. It should be noted that the liquid saturation is defined in the measurement and the predictions as the ratio of the total liquid water volume to the total pore volume in a GDL sample although liquid water may be unevenly distributed along the normal direction to the liquid injection surface of the sample. On the other hand, the liquid saturation in the transport simulation is considered to be the ratio of the average local volume of liquid water to the average local volume of pore. It is also important to note that the capillary pressure could not be measured or predicted above a liquid saturation level of about 0.1, and the relative permeability of the liquid phase could not be predicted under a liquid saturation level of 0.2, as described in the previous section. In order for these parameters to be applied to the macroscopic approach, we have extrapolated the data in Figs. 9 and 10 to fit the empirical equations. The fitted correlations are shown in Figs. 12 and 13 and they are described as Eqs. (8)–(10). The correlated capillary pressure is as follows:

$$P_c = \begin{cases} 2.4 \times 10^6 s^2 - 2.5 \times 10^5 s & 0 \le s < 0.05 \\ -10^4 s - 6 \times 10^3 & 0.05 \le s < s_a < 1 \end{cases}, \quad (8)$$

where s_a is the upper bound of the applicable range of Eq. (8). The capillary pressure curve decreases linearly after $s > 0.05$, there has to be inflection point somewhere before $s = 1$ and the capillary pressure has to decrease sharply. This is because it needs big liquid pressure to force liquid into the remained small pores near $s = 1$. The inflection point could not be measured experimentally in this study and the value s_a is not clear at this point. And the correlated relative permeabilties are as follows:

$$k_{rl} = \mathrm{MAX}(1.089(s^{1.5} - 1) + 1, 0), \quad (9)$$

$$k_{rg} = (1 - s)^5. \quad (10)$$

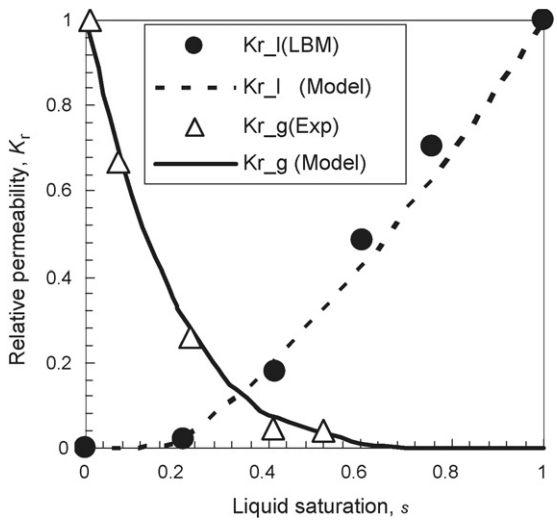

Fig. 13. Measured and predicted relative permeability and correlated model.

We define MAX(A, B) to denote the greater of A and B in Eq. (9). And the relative permeability of the liquid phase is 0 when saturation is small in this expression. As shown in Table 6, the liquid saturation at the gas channel end ($x = L$) was set to be 0.2. Since we found no direct in situ measurement on saturation in the GDL at the channel interface in past research, a realistic value was set for the first try to demonstrate the simulation method. This value was set because an in situ observation of a PEMFC shows that the liquid droplets are covering some portion of the GDL surface [34].

Fig. 14 shows computational results for the species concentration and liquid saturation. The water vapor concentration is constant because isothermal condition is assumed. The liquid saturation is high at the catalyst layer end ($x = 0$) due to water generation, while the oxygen concentration is low due to consumption. Similar states can be seen in the pressure profiles of the both liquid and gas phases as shown in Fig. 15. The liquid phase pressure is high, due to the water generation, while the gas phase pressure shows an opposite profile, due to the oxygen consumption. The pressure in the figure is the pressure difference from the reference state, which is the gas phase pressure at the gas channel end ($P_g|_{x=L}$). Note that the liquid phase pressure

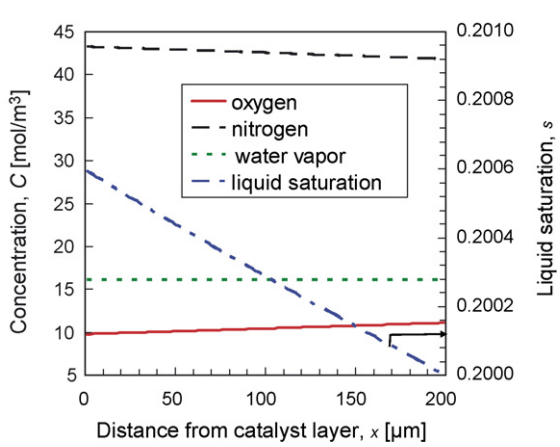

Fig. 14. Distributions of species concentration and liquid saturation.

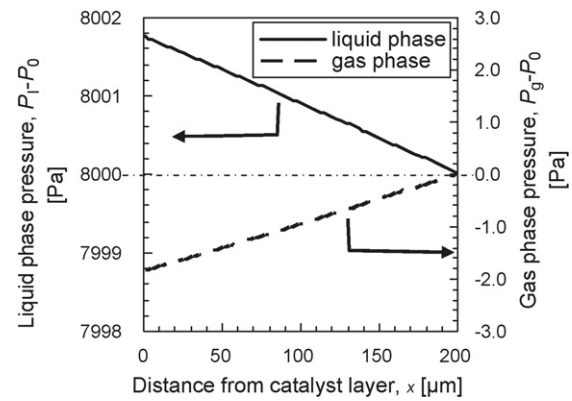

Fig. 15. Pressure distributions of liquid phase and gas phase.

is higher than the gas phase pressure by the capillary pressure as in Eq. (7).

The mass flux and intrinsic local mass average velocity [35] were extracted from the computational result at the middle point ($x = L/2$) to identify in detail the transport phenomenon in the GDL. The intrinsic velocity of phase k and species α in the gas phase are deduced by Eqs. (11) and (12), respectively:

$$u_{\mathrm{Int},k} = \frac{u_k}{(1-s)\varepsilon}, \tag{11}$$

$$u^{\alpha}_{\mathrm{Int,g}} = \frac{n^{\alpha}_{\mathrm{g}}}{C^{\alpha}_{\mathrm{g}} M^{\alpha}(1-s)\varepsilon}. \tag{12}$$

The results are summarized in Table 7, which shows that the gas phase mass flux is negative and that it flows from the gas channel end to the catalyst layer end, as opposed to the liquid phase, which flows from the catalyst layer end to the gas channel end. Oxygen, due to its larger concentration gradient, moves much faster than the gas phase. Water vapor moves slowly to the catalyst layer along with the advection of the gas phase mixture which is caused by the gas phase pressure gradient although no diffusion due to concentration gradient occurs. Although nitrogen does not move in the macroscopic sense, the diffusion velocity, which is the difference between the velocity of the species and the gas phase velocity, is positive. This means that the positive diffusion and negative advection are balanced. Compared to the liquid phase water mass flux, transported gas phase flux is around half in the reverse direction. And the gas phase water flux is negligible.

Table 7
Mass flux and velocity in GDL at $x = L/2$

Phase	Mass flux (kg m^{-2} s^{-1})	Intrinsic velocity (m s^{-1})
Gas phase		
Mixture	$\rho_g u_g = -1.67 \times 10^{-3}$	$u_{\mathrm{Int,g}} = -1.44 \times 10^{-3}$
O_2	$n^{O_2}_g = -1.66 \times 10^{-3}$	$u^{O_2}_{\mathrm{Int,g}} = -7.73 \times 10^{-3}$
H_2O	$n^{H_2O}_g = -1.57 \times 10^{-5}$	$u^{H_2O}_{\mathrm{Int,g}} = -8.44 \times 10^{-5}$
N_2	$n^{N_2}_g = 0$	$n^{N_2}_{\mathrm{Int,g}} = 0$
Liquid phase		
Water	$\rho_l u_l = 3.75 \times 10^{-3}$	$u_{\mathrm{Int,l}} = 2.40 \times 10^{-5}$

Although this transport simulation model of the two-phase flow properties of GDL needs to be developed further to incorporate the thermal effect and the effect when coupled with other layers, it does provide insight into the hidden phenomena of a GDL. Experimental validation of the calculated saturation is also desirable.

4. Conclusions

We have proposed a series of methods to analyze the transport phenomena involved in liquid–gas two-phase multi-component flow in the GDL of a PEMFC. These methods were applied to measure the capillary pressure and relative permeability of the gas phase in an actual carbon-fiber paper GDL, to predict the capillary pressure and relative permeability for both phases in the GDL, and to simulate two-phase multi-component flow in the GDL. The methods are applied to a carbon-fiber paper GDL considering the microstructure and the wettability of the GDL.

The predicted capillary pressure and relative permeability correctly estimated the shape of the curve of the measured results and showed similar magnitude. Transport simulation was carried out with the properties to identify the two-phase multi-component transport in the GDL.

Acknowledgment

The authors wish to thank C.Y. Wang for helping us understand the multi-phase mixture model in detail.

References

[1] J. St-Pierre, D.P. Wilkinson, S. Knights, M. Bos, J. New Mater. Electrochem. Syst. 3 (2000) 99–106.
[2] Z.H. Wang, C.Y. Wang, K.S. Chen, J. Power Sources 94 (2001) 40–50.
[3] U. Pasaogullari, C.Y. Wang, J. Electrochem. Soc. 151 (2004) A399–A406.
[4] U. Pasaogullari, C.Y. Wang, Electrochim. Acta 49 (2004) 4359–4369.
[5] U. Pasaogullari, C.Y. Wang, J. Electrochem. Soc. 152 (2005) A380–A390.
[6] U. Pasaogullari, C.Y. Wang, K.S. Chen, J. Electrochem. Soc. 152 (2005) A1574–A1582.
[7] H. Meng, C.Y. Wang, J. Electrochem. Soc. 152 (2005) A1733–A1741.
[8] G. Lin, W. He, T.V. Nguyen, J. Electrochem. Soc. 151 (2004) A1999–A2006.
[9] T.V. Nguyen, W. He, in: W. Vielstich, A. Lamm, H.A. Gasteiger (Eds.), Handbook of Fuel Cells—Fundamentals, Technology and Applications, vol. 3, John Wiley & Sons, 2003, p. 325.
[10] G. Lin, T.V. Nguyen, J. Electrochem. Soc. 153 (2006) A372–A382.
[11] J.H. Nam, M. Kaviany, Int. J. Heat Mass Transfer 46 (2003) 4595–4611.
[12] C.Y. Wang, Chem. Rev. 104 (2004) 4727–4766.
[13] F.A.L. Dullien, Porous Media: Fluid Transport and Pore Structure, second ed., Academic Press, 1992.
[14] J.T. Gostick, M.W. Fowler, M.A. Ioannidis, M.D. Pritzker, Y.M. Volfkovich, A. Sakars, J. Power Sources 156 (2006) 375–387.
[15] H. Ohn, T. Nguyen, Proton Exchange Membrane Fuel Cells V, Electrochemical Society Meeting, Los Angeles, CA, Paper # 1013, October 16–21, 2005.
[16] C.Y. Wang, P. Cheng, Adv. Heat Transfer, vol. 30, Academic Press, 1997, p. 93.
[17] C.Y. Wang, Numer. Heat Transfer B: Fundam. 31 (1997) 85.
[18] M. Kaviany, Principles of Heat Transfer in Porous Media, second ed., Springer, New York, 1999.
[19] M.F. Mathias, J. Roth, J. Fleming, W. Lehnert, in: W. Lietsich, A. Lamm, H.A. Gasteiger (Eds.), Handbook of Fuel Cells—Fundamentals, Technology and Applications, vol. 3, John Wiley & Sons, 2003, p. 517, Part 3.
[20] F.A.L. Dullien, C. Zarcone, I.F. Macdonald, A. Collins, R.D.E. Bochard, J. Colloid Interface Sci. 127 (2) (1989) 362.
[21] S. Bekke, P.E. Oren, SPE J. 2 (1997) 136–149.
[22] R.G. Hughes, M.J. Blunt, Adv. Water Resour. 24 (2001) 409–421.
[23] J. Toriwaki, Three Dimensional Digital Image Processing, Shokoudo Press, Japan, 2002.
[24] W.B. Lindquist, J. Geophys. Res. 101 (B4) (1996) 8297–8310.
[25] J.G. Richardson, J.K. Kerver, J.A. Hafford, J.S. Osoba, Petrol. Trans. AIME 195 (1952) 187.
[26] F.G. McCaffery, D.W. Bennion, J. Can. Petrol. Tech. 13 (1974) 42.
[27] E. Dana, F. Skoczylas, Int. J. Multiphase Flow 28 (2002) 1719–1736.
[28] H. Li, C. Pan, C.T. Miller, Phys. Rev. E 72 (2005), 026705.
[29] C. Pan, M. Hilpert, C.T. Miller, Water Resour. Res. 40 (2004), W0150110.
[30] X. Shan, H. Chen, Phys. Rev. E 47 (3) (1993) 1815–1819.
[31] X. Shan, H. Chen, Phys. Rev. E 49 (4) (1994) 2941–2948.
[32] Y.H. Qian, D. d'Humieres, P. Lallemand, Europhys. Lett. 17 (1992) 479–484.
[33] S.V. Patankar, Numerical Heat Transfer and Fluid Flow, Hemisphere, 1980.
[34] F.Y. Zhang, X.G. Yang, C.Y. Wang, J. Electrochem. Soc. 153 (2006) A225–A232.
[35] R.B. Bird, W.E. Stewart, E.N. Lightfoot, Transport Phenomena, John Wiley & Sons, 1960.